LASER & PHOTONICS REVIEWS

www.lpr-journal.org

Multimetallic Metasurfaces for Enhanced Electrocatalytic Oxidations in Direct Alcohol Fuel Cells

Rambabu Yalavarthi, Omer Yesilyurt, Olivier Henrotte, Štěpán Kment, Vladimir M. Shalaev, Alexandra Boltasseva, and Alberto Naldoni**

Plasmonic metasurfaces enable unprecedented manipulation of light by using periodic arrangement of resonant unit cells or nanoantennas. Here, multimetallic metasurfaces made of self-standing Ni/Au-Pt nanostructured films are shown to significantly enhance an electrocatalytic oxidation reaction employed in direct alcohol fuel cells. The Ni/Au metasurfaces support photonic and plasmonic modes, which are leveraged for the site-selective deposition of Pt electrocatalysts within the electromagnetic hot spots, where their reactivity can be strongly increased. The enhanced electrocatalytic activity for the methanol oxidation reaction (MOR) is primarily attributed to electronic effects due to the excitation of hot charge carriers and plasmonic near fields, as supported by electromagnetic simulations and kinetic isotopic experiments. Wavelength-dependent photoelectrochemical investigations suggest that Ni/Au-Pt metasurfaces enhances MOR over a broad spectral range and favors different light-induced reaction mechanisms depending on the selected energy window.

1. Introduction

Direct alcohol fuel cells (DAFCs) offer a promising solution to generate clean electricity from the electrochemical oxidation of alcohols such as methanol, ethanol, ethylene glycol, and glycerol.[1–3] The main advantage of DAFCs is the usage of alcohols since they can be retrieved from biomass conversion at low costs.[4] Moreover, they are secure and convenient to transport and store compared to hydrogen. However, the low redox efficiency owing to sluggish reaction kinetics of electrode materials has impeded the full-fledged commercialization of DAFCs.[2,3,5] In this regard, noble (Pt, Pd, and Rh) and non-noble metal (Ni, Co, and Mn) electrocatalysts have been employed to improve the slow kinetics for the alcohol oxidation reaction (AOR).[2] Among all, platinum is the benchmark electrocatalyst material for DAFCs due to its excellent activity, robustness, and more negative AOR onset potential. However, the use of Pt poses issues of device scalability, CO poisoning, and manufacturing costs.[2] Thus, alternative materials and approaches to minimize the usage of Pt are needed to reduce the operational costs of DAFCs.[2,6,7] The most relevant type of DAFC is based on the methanol oxidation reaction (MOR). In this context, the coupling of MOR electrocatalysts with plasmonic (metallic) nanostructures has shown great potential in accelerating the reaction kinetics. Existing reports on plasmon-assisted MOR have been limited to colloidal plasmonic nanostructures exhibiting localized surface plasmon resonances (LSPRs),[8–14] while the use of planar, ultra-thin metasurfaces—employing specially engineered arrays of plasmonic units/nanoantennas—for MOR remained unexplored. LSPRs occur in metallic/plasmonic nanostructures when the oscillation of conducting electrons on a metal surface is excited by a photon with an energy resonant to the frequency of electrons' collective motion. Plasmonic nanostructures concentrate light into subwavelength volumes and generate highly intense and localized near fields, so-called "hot spots". In the case of plasmon-enhanced catalysis, the optical near fields, resulting in non-thermal ("hot") charge carriers, and local heating can accelerate chemical reactions.[15–22] The operational spectral range of plasmonic nanocatalysts is determined by their shape and size, with the excited optical resonances often limited to LSPRs. In contrast, plasmonic metasurfaces offer exciting opportunities in tailoring optical response by designing periodic arrays of plasmonic units on planar substrates.[23–25] The unit cell symmetry and the substrate properties provide new degrees of freedom to design electromagnetic (EM) properties, which cannot be supported by simple metallic nanostructures.

Here, we employ multimetallic metasurfaces as a robust electrode material for plasmon-enhanced MOR (**Figure 1**). By using a scalable fabrication approach, we developed large area (centimeter-scale) photoanodes utilizing Ni, an Earth-abundant and low-cost element, whose optical properties where modified

R. Yalavarthi, O. Henrotte, Š. Kment, A. Naldoni
Czech Advanced Technology and Research Institute
Regional Centre of Advanced Technologies and Materials
Palacký University
Slechtitelů 27, Olomouc 78371, Czech Republic
E-mail: alberto.naldoni@upol.cz

O. Yesilyurt, V. M. Shalaev, A. Boltasseva
School of Electrical & Computer Engineering and Birck Nanotechnology Center
Purdue University
West Lafayette, IN 47907, USA
E-mail: aeb@purdue.edu

The ORCID identification number(s) for the author(s) of this article can be found under https://doi.org/10.1002/lpor.202200137

DOI: 10.1002/lpor.202200137

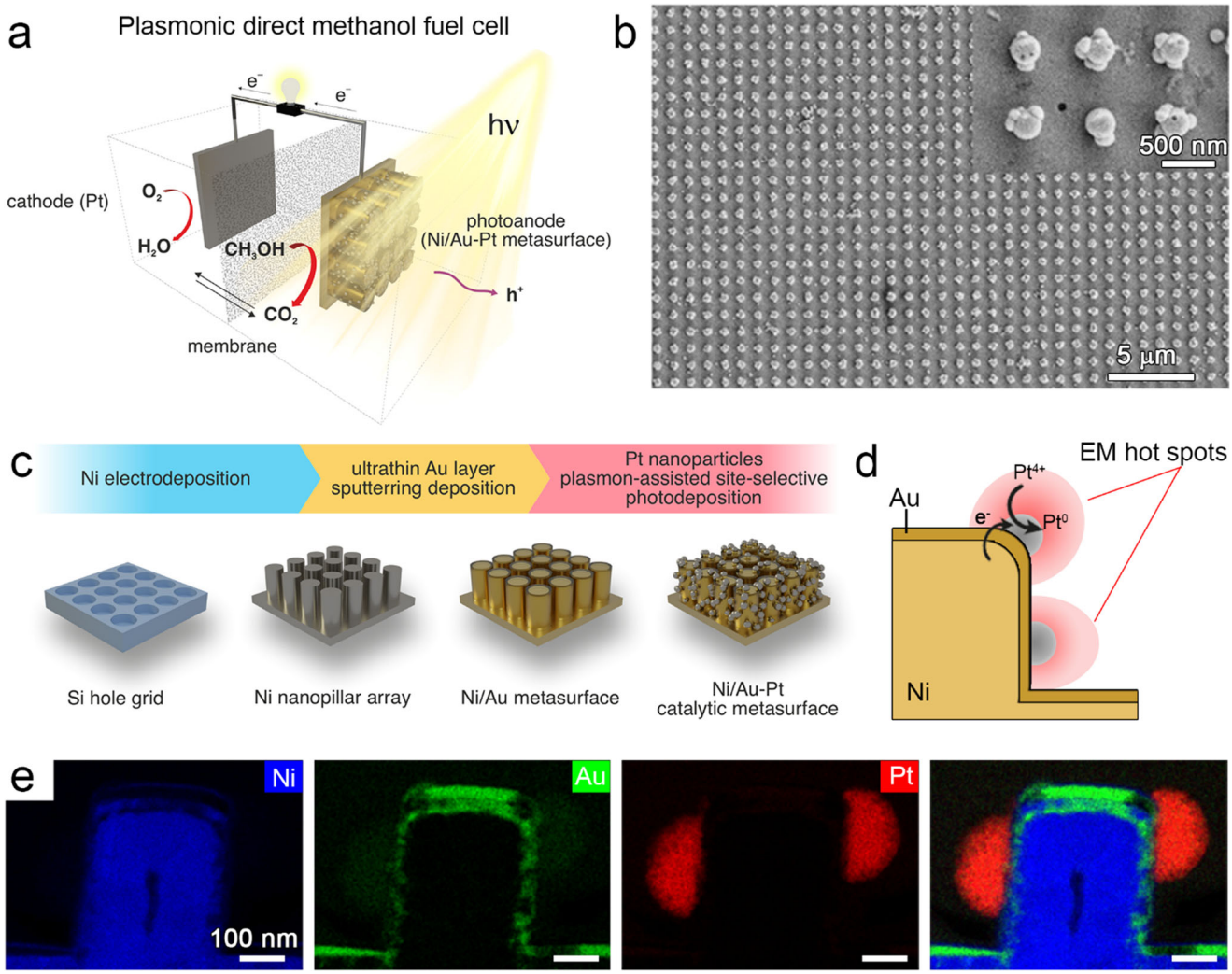

Figure 1. a) Schematic representation of a plasmonic direct methanol fuel cell employing a Ni/Au-Pt metasurface as the photoanode. b) Large area and enlarged view (inset) FE-SEM images of a Ni/Au-Pt metasurfaces (pitch = 800 nm, Au = 30 nm, Pt = 90 min). c) Fabrication scheme of the catalytic Ni/Au-Pt metasurfaces. d) Schematic representation of EM hot spot-mediated deposition of Pt nanoparticles over the plasmonic Ni/Au metasurfaces. e) EDS elemental maps of Ni, Au, Pt, and joined Ni-Au-Pt for a Ni/Au-Pt metasurfaces (pitch = 800 nm, Au = 30 nm, Pt = 90 min). Scale bar corresponds to 100 nm in all the images. The Ni/Au-Pt metasurfaces with 400 and 800 nm pitches are hereinafter labeled as Ni/Au-Pt@400 and Ni/Au-Pt@800, respectively.

by depositing thin layers of Au by sputtering (10–40 nm). Experimental measurements and EM simulations show that the obtained Ni/Au metasurfaces support a rich set of optical resonances, which enabled a broadband absorption over the entire visible and near-infrared spectral ranges. In the last fabrication step, we used the EM hot spot generated by the plasmonic resonances to drive the site-selective deposition of Pt nanoparticles. Such unique Ni/Au-Pt metasurfaces strongly enhanced the electrocatalytic MOR activity of Pt under external illumination. We investigate the MOR enhancement for different array pitches, Au thickness, and Pt deposition time. Furthermore, we present sets of experiments, including temperature-dependent under dark and kinetic isotopic MOR, which enabled to disentangle the contributions of photothermal heating, hot charge carriers, and electromagnetic near fields to the reaction mechanism.

2. Results and Discussion

2.1. Fabrication of Catalytic Ni/Au-Pt Metasurfaces

The plasmonic photoanodes including Ni/Au-Pt metasurfaces with 400 and 800 nm pitches were fabricated following the approach illustrated in Figure 1c. First, self-standing centimeter-scale Ni nanopillar (200 nm diameter, 350 nm height) array films were prepared using a Si hole grid mask and an electrodeposition method.[26] The optical properties of the Ni nanostructures were modified by depositing Au thin layers of varying thicknesses (10 to 40 nm), with the aim of strengthening their metallic character and therefore enhancing plasmonic hot spots.[27] Finally, we deposited catalytic Pt nanoparticles onto the Ni/Au nanopillars using a plasmon-assisted photo-reduction method in an aqueous solution of H_2PtCl_6 under light illumination (AM 1.5G 100 mW

cm^{-2}). During the process of deposition, hot electrons generated at the EM hot spots present over the nanopillars' surface reduced the surface adsorbed chloroplatinic acid ions (Equation 1), thus directing the site-selective growth of Pt nanoparticles.[28] The oxidation reaction involving the hot holes may include both chlorine gas evolution and water oxidation.

$$PtCl_6^{2-} + 4e_{hot}^- \rightarrow Pt^0 + 6Cl^- \quad (1)$$

The loading of Pt nanoparticles was controlled by varying the deposition time from 30 to 120 min. The final Ni/Au-Pt metasurfaces presented a crystalline structure as evidenced by the representative X-ray diffraction (XRD) pattern (Ni/Au-Pt@800) reported in Figure S1, Supporting Information, which shows the predominant (111) and (200) peaks belonging to the Ni core, the (111) and (200) reflections of the Au shell, and the additional small peaks corresponding to the (111) and (200) planes of Pt nanoparticles. The morphology and the array geometry of the plasmonic metasurfaces were examined after each fabrication step and the corresponding scanning electron microscope (SEM) images show a remarkable long-range order over large areas (Figure 1b and Figures S2–S4, Supporting Information) for all the prepared films. The morphology of each component forming a Ni/Au-Pt metasurface can be better appreciated by looking the high resolution transmission electron microscopy (HRTEM) images obtained by energy-dispersive X-ray spectroscopy (EDS) elemental mapping of a film lamella obtained by focused ion beam cutting (Figure 1e and Figure S5, Supporting Information). The EDS elemental maps confirmed the successful sequential fabrication of Ni nanopillars coated with a thin Au shell (≈30 nm).

The Au layer coating the lateral surfaces of the Ni nanostructures appears to be less thick than that covering the planar surfaces, probably due to shadowing effects occurring during the sputtering deposition. Notably, Pt nanoparticles with diameters in the range of 50–100 nm were selectively deposited onto the corners and the lateral surfaces of the Ni/Au nanopillars, that is, at those locations where the plasmonic near fields show the highest intensity (see **Figure 2** and discussion below). This approach enables the minimization of the Pt loading, while locating the catalytic nanoparticles only in those areas where their reactivity can be manipulated using surface plasmon resonances.

2.2. Optical Properties of Catalytic Ni/Au-Pt Metasurfaces

The optical properties of the fabricated metallic nanoantenna arrays were investigated using UV–vis–NIR diffuse reflectance spectroscopy to measure the total reflectance (R) and obtain absorption (A) spectra as $A = 1 - R$ (see Figure 2a and Figure S6, Supporting Information). The Ni@400 nanopillar arrays show a strong broadband absorption over the whole vis–NIR wavelength range (Figure S6a, Supporting Information), reaching values above 0.9 in the 400–500 nm spectral region. In contrast, Ni@800 nanopillar films exhibit an absorption of 0.3 at similar wavelength in the visible, while denoting an additional peak centered at ≈900 nm (Figure 2a). The higher absorption of Ni@400 film is assigned to its higher fill factor compared to Ni@800, that is, a higher number of metallic nanoantennas per unit surface area. Interestingly, in all investigated cases the deposition of thin Au layers of varying thicknesses (10 to 40 nm) produced Ni/Au metasurfaces with modified optical properties. For both the @400 and @ 800 series (Figures S6a and S6c, Supporting Information), the insertion of Au metallic layers having better plasmonic properties than Ni, produced the appearance of pronounced absorption shoulders peaking at ≈700 and ≈600 nm for Ni/Au@400 and Ni/Au@800 metasurfaces, respectively. In the latter case, two additional effects can be observed, which monotonically increased with the Au layer thickness. In the 400–500 nm region, the enhanced absorption (almost double than that of pure Ni) can be assigned to the increased surface coverage by Au, which improves the excitation efficiency of the higher order cavity modes at these wavelengths.[26] At longer wavelengths, that is, between 700 and 1100 nm, the deposition of Au thin shell produced a blue shift in the peak at ≈900 nm, and a monotonic decrease of background absorption, which we attributed to the increased reflectivity provided by the Au layer. After the hot spot mediated Pt deposition, the Ni/Au-Pt metasurfaces' spectra evidenced a broadening of the optical resonances (for both @400 and @800 series) and an increased background absorption at all wavelengths (only for @800 samples) (Figure 2a and Figures S6b and S6d, Supporting Information, for different Pt deposition time).

To understand the underlying plasmonic and photonic effects leading to the observed light absorption in Ni, Ni/Au and Ni/Au-Pt nanopillar arrays, we employed finite-difference time domain (FDTD) simulations. We focus our discussion on the samples with the 800 nm pitch, as they are the most active series in the plasmon-enhanced electrocatalytic methanol oxidation. Simulated absorption spectra and electric field distribution maps for metasurfaces with 400 nm and 800 nm pitch can be found in Supporting Information (Figures S7–S15 and Table S1–S2, which report the maximum electric field for each investigated configuration). In all cases, the absorption spectra show that the plasmonic metasurfaces support several cavity modes, which are mainly defined by the refractive index of the constituent materials, periodicity, and the nanopillar height. The observed optical resonances can be attributed to different excitations in different spectral regions. In the wavelength range 400–500 nm, the nanostructures support higher order cavity modes,[26] whose strength increased with a higher Au layer thickness, in agreement with the experimental data. Within 500 and 700 nm, a strong absorption peak due to hybrid photonic–plasmonic modes, from the coupling of the higher order cavity modes and surface plasmons,[26] emerges and well-matches with the measured absorption spectra. The latter (Figure 2a and Figure S6c, Supporting Information), however, show weaker resonances in comparison with the simulated spectra probably due to the uneven Au sputtering deposition on the lateral nanopillars' surface.

The electric field distribution maps for Ni@800 (Figure 2d) and Ni/Au (30 nm) (Figure 2e) metasurfaces at 600 nm evidence the enhancing effect of the Au shell on the plasmonic near fields. The same effect was observed for all the investigated Au thicknesses (Figure S12, Supporting Information), as well as for the Ni/Au@400 series (Figure S8, Supporting Information). In the third spectral range, that is, 700–1100 nm, the simulated spectra revealed a high-quality resonance reflected by the very intense and narrow peak appearing at ≈800 nm, which is evident both for Ni@800 and Ni/Au@800 metasurfaces (Figure 2b).

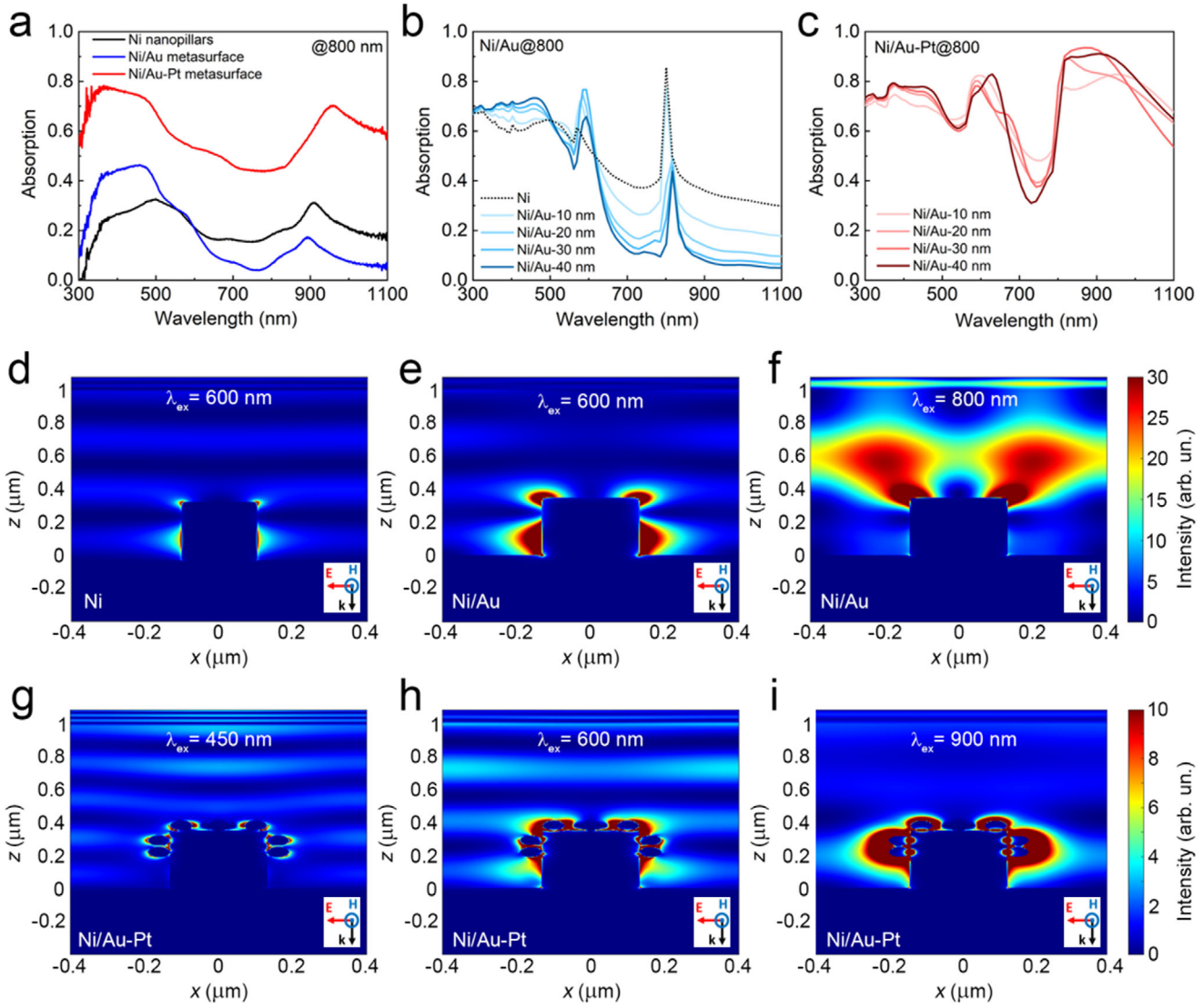

Figure 2. a) Experimental absorption spectra of Ni nanopillar array film (black line), Ni/Au (blue line) and Ni/Au-Pt (red line) metasurfaces (pitch = 800 nm, Au = 30 nm, Pt = 90 min). b,c) Simulated absorption spectra for Ni nanopillars (dotted black line) and a Ni/Au metasurface without and with Pt nanoparticles, respectively, for different values of the Au layer thickness (pitch = 800 nm) under linearly-polarized EM irradiation. Electric field intensity distribution maps for d) Ni nanopillars, e,f) Ni/Au metasurface, and g–i) Ni/Au-Pt metasurface samples with Au thickness of 30 nm, pitch = 800 nm, under monochromatic excitation at selected wavelengths. Polarization in all pictures lies parallel to the field maps.

The wavelength at which the resonance occurs equals to the periodicity of the unit cells and therefore it can be assigned to a surface lattice resonance (SLR), excited by the coupling between LSPRs and diffractive modes.[29] In the periodic array of plasmonic nanopillars, where the period is comparable to the wavelength of the incident light, under certain conditions the light scattered (diffracted) from one nanostructure can arrive in phase with the LSPR supported by its neighbor, thereby significantly increasing the quality factor of the resonance.[29,30] In the experimental spectra (Figure 2a), the SLRs are broadened due to the loss of symmetry induced by structural imperfections that may result from both the electrodeposition and strip-off fabrication steps. In all the electric field distributions of Ni@800 (Figure S13, Supporting Information) and Ni/Au@800 metasurfaces (Figure 2f and Figure S14, Supporting Information) at 800 nm excitation wavelength, the field is concentrated above the metallic nanopillar, which is different from a conventional LSPR where the fields are localized around the unit cell. On the other hand, SLRs are known to possess such a field distribution where the field is localized in the superstrate region.[30,31] Indeed, addition of Au coating clearly increases the field concentration in the superstrate region by enhancing the resonant behavior at the resonance wavelength. We leveraged this property of the studied Ni/Au metasurfaces to carry out the plasmon-mediated photodeposition of Pt nanoparticles, whose growth was driven in a site-selective fashion by the plasmonic hot spots (Figure 2 and Figure S5, Supporting Information). The deposition of Pt nanoparticles modified the absorption spectra of the samples by broadening the optical resonances (Figure 2c) at both 600 and 900 nm (Figure 2e–i and Figures S8–S15, Supporting

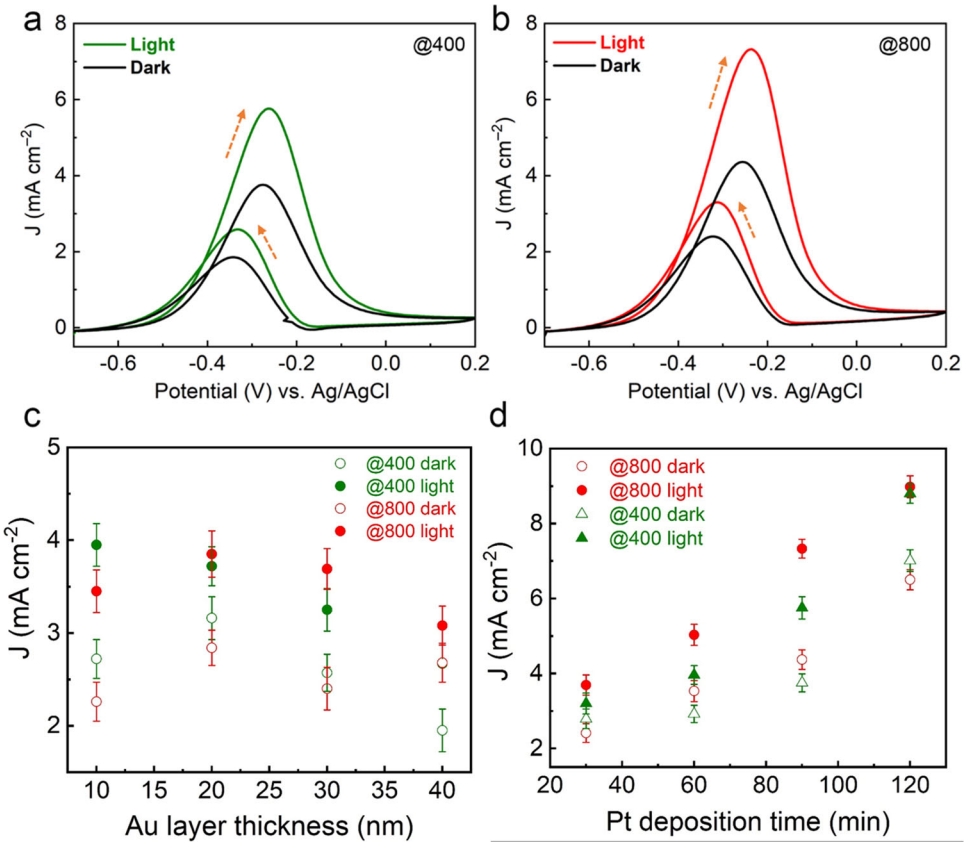

Figure 3. Cyclic voltammetry curves of MOR under dark and light conditions for Ni/Au-Pt metasurfaces (Au-30 nm, Pt-90 min) with a) pitch = 400 nm, and b) pitch = 800 nm. Arrows indicate the scan direction under both dark and light. MOR peak current optimization for Ni/Au-Pt metasurfaces with c) different Au layer thicknesses and same Pt deposition time (i.e., 30 min), and d) different Pt deposition times and same Au layer thickness (i.e., 30 nm). The MOR activity curves were measured in a mixed solution containing 0.5 M KOH and 0.5 M CH_3OH at room temperature and under simulated AM 1.5G solar light (100 mW cm^{-2}, one-sun).

Information). In particular, the high-quality SLRs were affected since the symmetry-dependent SLRs are compromised when asymmetric constituent elements are present. The field distribution maps are in accord with the observed absorption spectra and the validity of the SLR argument above. Moreover, the simulated field maps show that the optical near fields are concentrated around the Pt nanoparticles and that their strength follows the excitation wavelength order of 900 > 600 > 450 nm, with implications in the electrocatalytic mechanism for the MOR (see next section).

2.3. Plasmon-Enhanced Electrocatalytic Oxidation of Methanol

The electrocatalytic activity of the studied plasmonic metasurfaces was measured using a three-electrode electrochemical cell using an electrolyte solution with composition 0.5 M KOH/0.5 M CH_3OH. As expected, the Ni/Au metasurfaces did not show any significant MOR activity showing a peak at 0.8 V and only a 5% current increase under solar illumination (Figure S16, Supporting Information), thus we focused on the Ni/Au-Pt samples. The cyclic voltammetry (CV) curves of all Ni/Au-Pt samples showed two characteristic peaks, one appearing during the forward anodic scan, whereas the other peak growing during the reverse cathodic scan (**Figure 3**). The anodic scan peak centered at approximately –0.26 V is attributed to the oxidation of methanol, while the reverse scan peak at –0.35 V is assigned both to the oxidation of CO adsorbed on Pt to CO_2 and to the methanol oxidation triggered and counteracted by the reduction of PtO_x formed in the proceeding anodic scan.[32,33] Notably, Figure 3a,b shows that both the peaks were significantly enhanced upon light illumination, with one at –0.26 V monitored hereafter in more detail. The MOR activity of Ni/Au-Pt@400 under light illumination is enhanced by 52% in comparison to the dark signal, whereas for Ni/Au-Pt@800 the enhancement is 68%. It should be noted that, even though the Au thickness (30 nm) and Pt loading (90 min) are the same for both of the samples (and the dark current is similar), there is a significant difference in MOR activity under solar illumination.

We thoroughly characterized the plasmon-enhanced electrocatalytic activity in Ni/Au-Pt metasurfaces by systematically varying the Au film thickness (10–40 nm) and Pt deposition time (30–120 min) (see Figure 3c,d and Figures S17 and S18, Supporting Information, for complete CVs measurements). The dark current densities (J) for @400 series are slightly higher in comparison to those of the @800 metasurfaces, which can be attributed to the higher number of catalytic nanostructures present in the former films over the latter. In the case of Ni/

Au-Pt@400, the light-induced MOR activity follows a descendent trend with increasing the Au thickness.

In contrast, for the Ni/Au-Pt@800 samples, the trend reaches a maximum for 20 and 30 nm Au, and then decreases. Interestingly, this trend follows the same pattern revealed by the electric field distribution maps (Figure 2 and Figures S8–S15, Supporting Information), thus highlighting the tight connection between light-enhanced MOR activity and the optical resonances supported by the Ni/Au-Pt metasurfaces. Furthermore, Figure 3d shows the Pt loading optimization by keeping constant the Au thickness (30 nm). In this case, both @400 and @800 series show a MOR activity enhancement under light illumination for all Pt loadings, with the MOR activity increasing monotonically with the Pt deposition time (see the corresponding CVs in Figures S19 and S20, Supporting Information) due to the increased amount of catalytic sites (Pt atoms) available for electrocatalysis, as supported by the increasing roughness factors measured for all samples (Figure S21 and Table S3). Notably, a metasurface with the same composition Ni/Au-Pt and similar amount of active Pt (see Table S3), but with Pt deposited all over the metallic surface, did not show a significant light-induced catalytic enhancement as that seen for the sample prepared by plasmon-assisted Pt deposition onto the EM hot spots (Figure S22). Figure 3c,d shows that the @800 series presented higher light-induced enhancement in MOR in all investigated conditions, with the samples Ni/Au(30 min)-Pt(90 min)@800 having the highest activity increase among all samples. Therefore, we selected this plasmonic metasurface to systematically carry out mechanistic investigations and clarify the role of different plasmonic effects in manipulating the reactivity of Pt nanoparticles toward MOR.

Plasmonic nanostructures may enhance the kinetics of chemical reactions through the generation of photothermal heating, hot charge carriers, and EM near field enhancement. Hot charge carrier may be generated both by interband and intraband (i.e., plasmonic) transitions. The first type of electronic transitions occur from *d* states below the Fermi level to empty *sp* states above the Fermi level, when the excitation energy is above a certain threshold, which is 2.3–2.4 eV for Au[34–36] — the noble metal providing strong metallic character to our metasurfaces. Interband excitations do not require change in the momentum of the charge carriers, thus exhibiting large characteristic rate constant of $\approx 10^{15}$ s^{-1}.[34] Recently, the role of *d*-holes in directing Au photocatalysis and modifying intraband charge carrier kinetics has been highlighted.[37–39] In contrast, intraband transitions from *sp* filled states below the Fermi level to empty *sp* states above the Fermi level are generally available at all visible wavelengths for transition metals. They require a change in momentum of charge carriers, thereby showing a lower excitation rate constant of $\approx 10^{13}$ s^{-1}.[34] The momentum conservation can be broken by surface plasmons excitation and related processes such as electron–phonon coupling, electron scattering at defects or at the nanoparticle's surface.[40–43]

To discern the underlying mechanism of light-enhanced MOR activity, we tried to decouple the photothermal heating and hot carrier (and near field) contributions.

Figure 4a shows the temperature dependence of the MOR peak current density in dark conditions using electrolytes thermalized at different temperatures (see CVs in Figure S23, Supporting Information). The trend follows an Arrhenius-like exponential increase, as expected for thermally-driven chemical reactions. By measuring the temperature of the electrolyte before (20 °C) and after the CV measurements carried out under solar light (150 mW cm^{-2}) we detected a temperature gradient $\Delta T = 2$ °C. The variation of MOR activity under dark conditions for this ΔT corresponds to ≈0.8 mA cm^{-2} (Figure 4a), while using illumination at a power density of 150 mW cm^{-2}, the net enhancement J_{net} ($J_{dark} - J_{light}$) is ≈3 mA cm^{-2} (Figure 4b).

The intensity-dependent J_{net} trend follows a linear relationship, not only for the most performing sample, but also for all Ni/Au(30 min)-Pt metasurfaces functionalized with different Pt deposition time (not shown). The same behavior was observed both for the total peak current density and peak potential at increasing light intensities (Figure 4c). This result suggests that non-thermal charge carriers (and EM near fields) may play a prominent role in enhancing the MOR activity of Ni/Au-Pt metasurfaces, with a limited contribution deriving from photothermal heating. However, the limited heat removal in the electrochemical cell may result in local temperature gradients near the plasmonic metasurfaces leading to enhanced diffusion of reactive species, thereby potentially leading to the increased MOR activity under illumination.

Therefore, to investigate deeper this aspect, we compared the trend of peak potential as a function of the peak current density for both solar illumination and dark conditions (Figure 4d). The former produced a linear increase in the peak potential, while the latter produced an increase in current density but no change in the peak potential. This observation supports a mechanistic picture where the photothermal heating is not fully responsible for the enhanced electrocatalytic activity, with the electronic effects (hot carriers and near field) that play a role.[8]

To discern among the electronic effects influencing the MOR kinetics, we examined the energy-resolved electrocatalytic activity using light illumination at different wavelengths (**Figure 5**). The incident-to-photon conversion efficiency (IPCE) spectra, or action spectra, confirmed the higher performance of Ni/Au-Pt@800 in comparison to Ni/Au-Pt@400 metasurface, but also showed that the action spectrum of the former more closely resembled the feature of the absorption spectrum (Figure 5a,c). Notably, MOR measurements using light with different wavelengths (454, 540, 592, 656, 764, 865, and 950 nm) at an increasing power density for all the investigated energies and samples (@400 and @800, see Figure 5b,d) resulted in a linear dependence of J_{net} from the light intensity, observation which suggests again that electronic effects have a major influence on MOR.

Ni/Au-Pt@400 (Figure 5a) shows maximum IPCE values above 4% in the wavelength range 454–540 nm and a secondary peak at 764 nm with IPCE ≈2%. On the other hand, Ni/Au-Pt@800 (Figure 5c) reached three distinct IPCE maxima (≈6%) at 454, 656, and 950 nm. In the first energy region, the light-induced MOR activity under 454 nm, where the highest IPCE values are observed, can be assigned to *d* hot holes generated within the Au layer by interband transitions and subsequently transferred to the Pt nanoparticles, where the MOR occurs for both 400 and 800 pitch profiles.[17,38,44] This interpretation is supported by: i) the electric field distribution (Figure S15, and Figure S9 Supporting Information), which shows the smallest

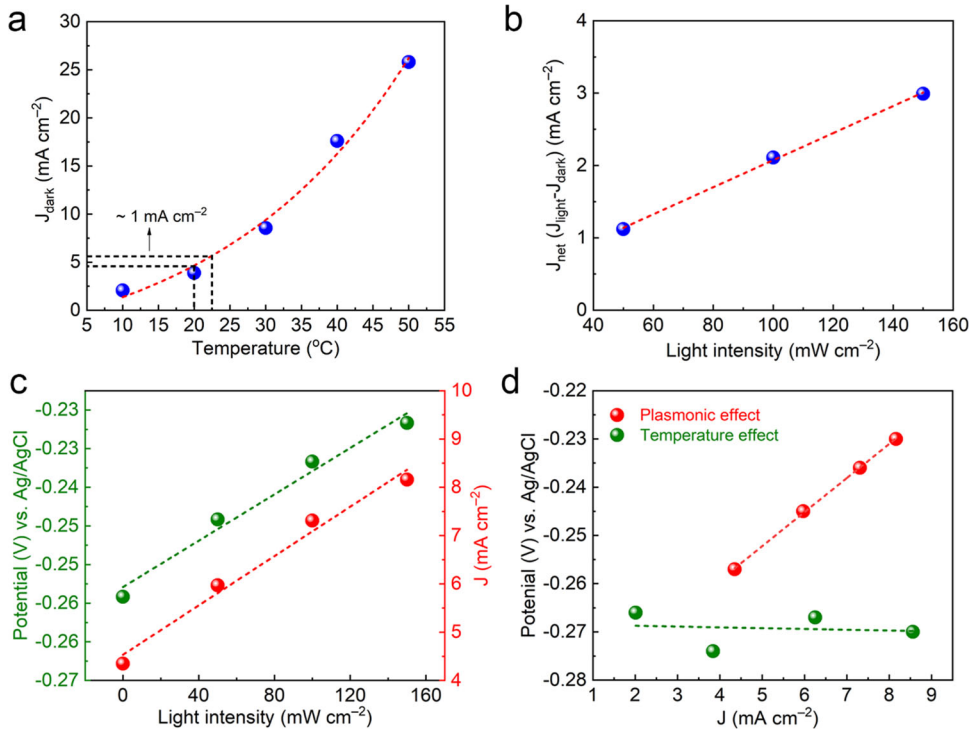

Figure 4. Role of electronic and temperature effects in the MOR for Ni/Au-Pt@800 metasurfaces (pitch = 800 nm, Au-30 nm, Pt-90 min). a) Peak current density in dark conditions at different temperatures. b) Net current density (J_{net}) obtained by subtracting the peak dark current density (J_{dark}) from the peak current density under light irradiation (J_{light}) at different solar light intensities. c) Peak potential (green circles) and current density (red circles) at different solar light intensities. (see also Figure S23c). d) Peak potential as a function of dark MOR activity (J) at different temperatures under dark conditions (green circles, derived from Figure S23a) and under light irradiation at different solar light intensities (red circles, derived from Figure S23c) and at constant temperature. The MOR activity curves were measured in a mixed solution containing 0.5 M KOH and 0.5 M CH_3OH at room temperature and under simulated AM 1.5G solar light.

enhancements at this wavelength; and ii) the fact that Au is weakly metallic (plasmonic) in this energy range. The high IPCE observed at longer wavelengths and peaking at 656 and 950 nm can be assigned to electronic effects (hot carriers and near fields) due to the plasmonic resonances supported by the Ni/Au-Pt@800 metasurfaces, as these are produced at energies below the Au interband transitions threshold. In contrast, for Ni/Au-Pt@400, the second IPCE maximum is observed at 764 nm and it is due to hybrid photonic plasmonic modes.

It should be noted that it is often challenging to discern and quantify the relative contributions due to plasmonic hot carriers and near fields, as the reaction rates exhibit a similar linear power response if enhanced by either one or the other effect, as observed in the present case for 656 and 950 nm (Figure 5d).[17,45] However, we suggest that at 656 nm plasmonic hot holes played a dominant role in enhancing the MOR kinetics.[46,47] After Pt deposition, indeed, the plasmonic metasurfaces still support the hybrid photonic–plasmonic modes, as can be appreciated by the electric field distribution maps in Figure S15, Supporting Information. In contrast, at 950 nm we assigned the MOR activity mainly to near field effects, as the Pt nanoparticles broke the structural lattice symmetry that enabled the SLRs in Ni/Au@800 metasurfaces (Figures S14 and S15, Supporting Information). Near fields may modify the adsorption/desorption strength of methanol, or reaction intermediates or products (i.e., CO), thus enhancing the overall MOR activity. The catalytic center of the MOR always remained the Pt nanoparticles, whose activity was enhanced alternatively by hot hole transfer or near fields, depending on the energy spectral range. A similar energy–resolved photochemistry has been recently observed for plasmonic metasurfaces using a single–particle investigation approach.[48]

Light–induced activity from the Pt nanoparticles can be excluded here since their size ranges between 50 and 100 nm and enhanced photocatalysis over Pt has been only observed for very small nanoparticles (1–3 nm in diameter) due to the photoexcitation of metal–adsorbate transitions.[49]

To further explore the hot hole contribution, we carried out kinetic isotope effect (KIE) experiments by replacing the methanol with deuterated methanol (CD_3OD) in the electrolyte. The KIE involves multiple electronic transitions: the hot holes can be scattered into an unoccupied molecular orbital of the methanol adsorbed onto the Pt surface. This favors a C—H distance different from that of the ground state, with the lighter isotope (H) that will move over a larger distance than the heavier isotope (D), because it is accelerated faster. When the hole transfers back to the Pt leaving the C—H bond in its ground state, the lighter isotope will have a higher bond length than that held in the equilibrium position and will therefore acquire more vibrational energy that is available for overcoming the reaction barrier, thus resulting in larger reaction rates for the lighter isotope.[50]

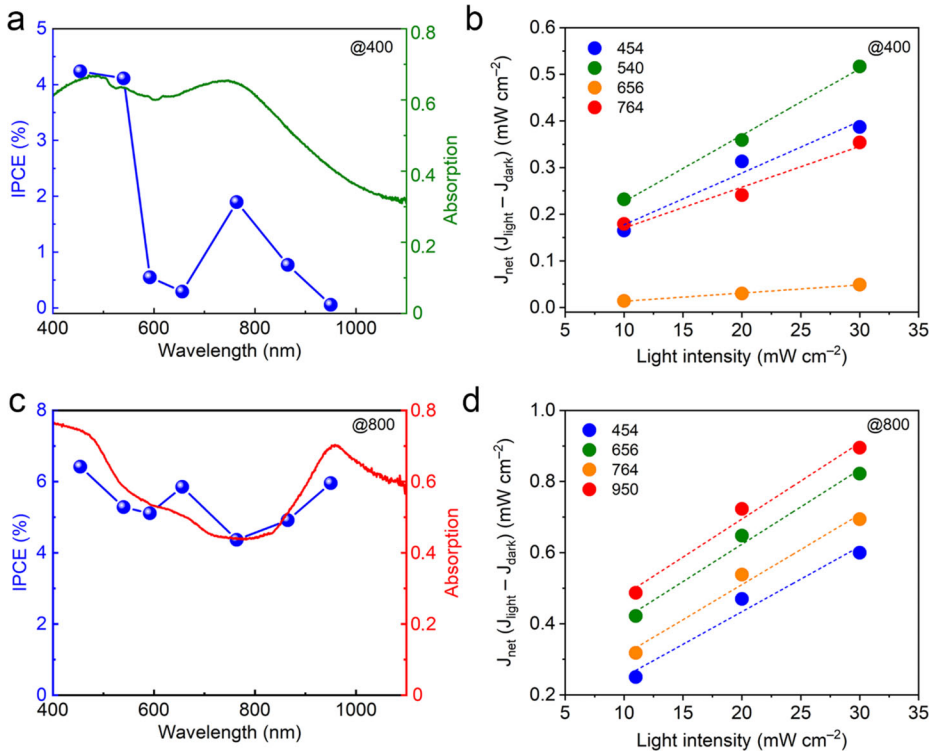

Figure 5. Incident-photon-to-current efficiency (IPCE%) for Ni/Au-Pt metasurfaces (Au-30 nm, Pt-90 min) with a) pitch = 400 nm and c) pitch = 800 nm, alongside with their absorption spectra. Net current density (J_{net}) obtained by subtracting the peak dark current density (J_{dark}) from the peak current density under light irradiation (J_{light}) using different monochromatic LEDs irradiation at different light intensities for Ni/Au-Pt metasurfaces with b) pitch = 400 nm and d) pitch = 800 nm. The MOR activity was measured in a mixed solution containing 0.5 M KOH and 0.5 M CH_3OH at a constant temperature of 10 °C.

The KIE for MOR can be expressed as follows:

$$KIE_{\text{dark}} = \frac{J(CH_3OH)_{\text{dark}}}{J(CD_3OD)_{\text{dark}}} \quad (2)$$

$$KIE_{\text{light}} = \frac{J(CH_3OH)_{\text{light}}}{J(CD_3OD)_{\text{light}}} \quad (3)$$

Figure S24, Supporting Information, shows the KIE CV plots for Ni/Au(30 nm)-Pt(90 min)@400 and Ni/Au(30 nm)-Pt(90 min)@800 metasurfaces, alongside Table S4, Supporting Information, summarizes KIEs for eight different samples under dark and light (one-sun) conditions. For thermally driven reactions, KIE is expected to be very small (≈1), that is, absence of an isotope effect. In contrast, all our experiments resulted in large KIE_{dark} values (Table S4, Supporting Information), denoting that MOR is an hole–mediated reaction and that the activation of C—H bonds is the rate-determining step.[50] Moreover, KIE_{light} values are constantly higher than KIE_{dark} ones, thus demonstrating the existence of a MOR pathway driven by hot carrier generated by Ni/Au-Pt plasmonic metasurfaces.[51] In addition, we performed open circuit potential (OCP) measurements to ascertain the plasmonic hot hole contribution in the methanol oxidation reaction. Figure S25 shows the OCP plot of Ni/Au-Pt@800 (Au -30 nm, and Pt- 90 min) under dark and illumination (100 mW cm^{-2}). The OCP shifts towards lower potentials within the time interval of minutes under illumination (shaded area) and starts increasing to the positive side once it reaches the lowest peak. The sudden decrease in OCP upon light illumination is attributed to the rapid build-up of negative potential on the surface of photoanode. The LSPR excitation generates plasmonic hot e^-–h^+ pairs and subsequent oxidation of methanol by hot holes and result the accumulation of electrons back on the pillar surface, which causes the negative shift in OCP upon light illumination. However, after few minutes, the OCP shifted towards the positive side and a steady state is achieved after several hundred minutes, which we attributed to the back recombination of e^-–h^+ pairs. The formation of this light-driven photopotential on the surface of the photoanode may also contribute to the enhanced metasurfaces reactivity by reducing the activation barrier of MOR.[52]

3. Conclusion

In summary, we proposed and experimentally realized self-standing Ni/Au-Pt plasmonic metasurfaces as photoanodes in direct methanol fuel cells and demonstrated broadband light-enhanced electrocatalytic activity for methanol oxidation. The plasmonic hot spot-mediated deposition of Pt nanoparticles over Ni/Au nanopillars enabled the use of optimized amounts of Pt and, at the same time, to locate Pt in the site-selective fashion over the areas where the light-induced enhancement could be maximized. A detailed mechanistic investigation on the nature of the

enhancement in the MOR revealed that the studied plasmonic metasurfaces offer the opportunity to enhance different reaction pathways in different spectral windows. We demonstrated that photothermal heating played a minor role in enhancing the methanol oxidation kinetics, while electronic effects, deriving from a rich variety of optical modes, were dominating. Specifically, hot carrier generation played a major role at higher energies (400–700 nm), whereas electromagnetic hot spots dominated in the NIR region. Our findings pave the way for the use of plasmonic metasurfaces for scalable solar-to-chemical energy conversion approaches, including various types of DAFCs and photoelectrochemical cells for the valorization of biomass derivatives.

4. Experimental Section

Fabrication of Ni/Au Metasurfaces: Silicon (Si) molds of different pitches (400 and 800 nm) with the same hole diameter of 200 nm and a hole etch depth of 350 nm were purchased from AMO GmbH. The electrodeposition technique was employed to prepare the Ni nanopillar array films. Initially, Si molds were cleaned in a piranha solution (3:1, H_2SO_4 to H_2O_2 volume ratio) to remove surface impurities. Subsequently, a gold layer (10 nm) was deposited on the surface of Si mold using magnetron sputtering to serve as a conductive layer for electrodeposition. An aqueous solution comprising of 0.12 M $NiCl_2$, 0.12 M $NiSO_4$, and 0.5 M H_3BO_3 (Merck) was used as an electrolyte for electrodeposition of Ni under the constant current density of 10 mA cm^{-2}. The as deposited Ni nanopillar arrays were carefully stripped off from the Si mold. Afterwards, a gold conformal layer of varying thickness (10, 20, 30, and 40 nm) was deposited onto their surface using magnetron sputtering to obtain the Ni/Au metasurfaces.

Deposition of Pt Nanoparticles on Ni/Au Metasurfaces: The photodeposition method was used to decorate Ni/Au metasurfaces with catalytic Pt nanoparticles. Briefly, the Ni/Au metasurfaces were immersed in a 0.1 mM aqueous solution of chloroplatinic acid ($H_2PtCl_6{\cdot}6H_2O$, Merck) and illuminated with simulated AM 1.5G solar light (100 mW cm^{-2}, one-sun) for various time intervals (30, 60, and 150 min) to achieve plasmonic hot spot-mediated Pt nanoparticle growth. Eventually, the as-fabricated Ni/Au-Pt metasurfaces were annealed in air at 300 °C for 1 h with heating and cooling rates of 2 °C min^{-1}.

Characterization: The morphology of Ni/Au-Pt metasurfaces was analyzed by a field emission scanning electron microscope (FE-SEM) Hitachi SU 6600 (Hitachi). An Empyrean (PANalytical) diffractometer equipped with a Co-Kα line ($\lambda = 0.1789$ nm) radiation source in the Bragg–Brentano configuration was used to collect the X-ray diffraction patterns. The UV–vis spectroscopy measurements were performed using a Specord 250 Plus spectrophotometer equipped with an integrating sphere (Analytik Jena GmbH, Germany). Absorption (A) was obtained by measuring the total reflectance (R) of the samples and using the formula $A = 1 - R$. Spectralon was used as a reference sample. A high-resolution transmission electron microscope (HRTEM), Titan G2 (FEI) at an accelerating voltage of 80 kV was used for TEM measurements and EDS mapping. BM UltraScan CCD camera (Gatan) was used to capture the elemental maps. The sample preparation was carried out on a FIB-SEM instrument Scios 2 DualBeam (ThermoFisher SCIENTIFIC). The area of interest was coated by tungsten (electron beam deposition) with a gas injection system (GIS). The sample was tilted by 52° and the milling procedure was performed in order to get the lamella from the bulk sample. The lamella was undercut and removed from the bulk material by micromanipulator and attached to the TEM grid. After the welding of lamella to the grid, the lamella was thinned by ion milling using several steps with decreasing currents until it was transparent to the accelerated electron beam.

Photoelectrochemical Measurements: A Gamry series G 300 potentiostat (Gamry Instruments, USA) was used to carry out cyclic voltammetry measurements aided with a standard three-electrode photoelectrochemical cell in a mixed electrolyte solution of 0.5 M KOH and 0.5 M CH_3OH. Ni/Au-Pt metasurfaces were used as the working electrode, a Pt wire was the counter electrode, and an Ag/AgCl (3 M KCl) was the reference electrode. A Xenon lamp (150 W) equipped with an AM 1.5G filter was used as a light source with a light intensity of 100 mW cm^{-2} (one-sun). Incident photon-to-current efficiency (IPCE) measurements were carried out using a Zahner PP 211 IPCE setup equipped with LEDs of different wavelengths. The IPCE was calculated as follows:

$$\mathrm{IPCE}(\%) = \frac{J_\lambda \times 1240}{P_\lambda \times \lambda} \times 100 \tag{4}$$

where J_λ is the difference in photocurrent density of dark and light measured under illumination at λ, λ is the incident light wavelength, and P_λ refers to the power density measured at a specific wavelength. Intensity-dependent photocurrent measurements were performed using the different LEDs available within the Zahner PP 211 photoelectrochemical station.

Numerical Simulations: Full-wave finite-difference time domain (FDTD) simulations were performed using a commercial 3D Maxwell solver (Lumerical software). A single unit cell was simulated using periodic boundary conditions in the in-plane dimensions and perfectly matched layers in the out-of-plane dimension. The excitation beam was set as a linearly x-polarized plane wave that spectrally covers 300–1100 nm wavelength range. The geometric dimensions of the Ni nanopillars (i.e., periodicity of 400 and 800 nm, height of 350 nm, diameter of 200 nm) were set according to the experimental characterization. The thickness of the Au coating was used as the sweeping parameter (from 10 to 40 nm) during simulations. For the case with Pt nanoparticles, Pt spheres with 60 nm diameter were randomly placed on and around the Au coated Ni nanopillar. In order to capture field evolution in the regions close to the unit cell and the nanogaps such as the space between spheres or spheres and Ni pillar, we used a very dense mesh with 3 nm steps in all directions. The structures were modeled using fully dispersive optical material properties for nickel,[53] gold,[54] and platinum.[26]

Supporting Information

Supporting Information is available from the Wiley Online Library or from the author.

Acknowledgements

The authors gratefully acknowledge the support from the Ministry of Education, Youth and Sports through the Operational Programme Research, Development and Education - European Regional Development Fund, project no. CZ.02.1.01/0.0/0.0/15_003/0000416. A.N. acknowledges the support from the Czech Science Foundation (GACR) through the projects 20–17636S and 22-26416S. Purdue co-authors acknowledge the support from National Science Foundation (NSF) under award 2029553-ECCS. The authors acknowledge J. Hošek and O. Tomanec for the lamella preparation and EDS mapping, respectively.

Conflict of Interest

The authors declare no conflict of interest.

Data Availability Statement

The data that support the findings of this study are available in the Supporting Information of this article.

Keywords

electromagnetic near fields, fuel cells, hot carriers, metasurfaces, plasmonic photoelectrochemistry

Received: March 3, 2022
Published online: April 28, 2022

[1] K. V. Kordesch, G. R. Simader, *Chem. Rev.* **1995**, *95*, 191.
[2] N. Kakati, J. Maiti, S. H. Lee, S. H. Jee, B. Viswanathan, Y. S. Yoon, *Chem. Rev.* **2014**, *114*, 12397.
[3] H. Liu, C. Song, L. Zhang, J. Zhang, H. Wang, D. P. Wilkinson, *J. Power Sources* **2006**, *155*, 95.
[4] H. Luo, J. Barrio, N. Sunny, A. Li, L. Steier, N. Shah, I. E. L. Stephens, M. Titirici, *Adv. Energy Mater.* **2021**, *11*, 2101180.
[5] M. K. Debe, *Nature* **2012**, *486*, 43.
[6] Z. Wang, J. Du, Y. Zhang, J. Han, S. Huang, A. Hirata, M. Chen, *Nano Energy* **2019**, *56*, 286.
[7] X. Yang, Q. Wang, S. Qing, Z. Gao, X. Tong, N. Yang, *Adv. Energy Mater.* **2021**, *11*, 2100812.
[8] L. Huang, J. Zou, J. Ye, Z. Zhou, Z. Lin, X. Kang, P. K. Jain, S. Chen, *Angew. Chem., Int. Ed.* **2019**, *58*, 8794.
[9] S. Lee, Y. Wy, Y. W. Lee, K. Ham, S. W. Han, *Small* **2017**, *13*, 1701633.
[10] H. Xu, P. Song, J. Wang, F. Gao, Y. Zhang, J. Guo, Y. Du, J. Di, *ChemElectroChem* **2018**, *5*, 1191.
[11] Z. Zheng, T. Tachikawa, T. Majima, *J. Am. Chem. Soc.* **2014**, *136*, 6870.
[12] Y. Liu, F. Chen, Q. Wang, J. Wang, J. Wang, T. T. Gebremariam, *J. Mater. Chem. A* **2018**, *6*, 10515.
[13] H. Xu, P. Song, J. Wang, Y. Shiraishi, Y. Du, Q. Liu, *ACS Sustainable Chem. Eng.* **2018**, *6*, 7159.
[14] J. Bi, H. Cai, B. Wang, C. Kong, S. Yang, *Chem. Commun.* **2019**, *55*, 3943.
[15] L. Mascaretti, A. Dutta, Š. Kment, V. M. Shalaev, A. Boltasseva, R. Zbořil, A. Naldoni, *Adv. Mater.* **2019**, *31*, 1805513.
[16] A. Naldoni, V. M. Shalaev, M. L. Brongersma, *Science* **2017**, *356*, 908.
[17] R. Kamarudheen, G. J. W. Aalbers, R. F. Hamans, L. P. J. Kamp, A. Baldi, *ACS Energy Lett.* **2020**, *5*, 2605.
[18] A. O. Govorov, H. H. Richardson, *Nano Today* **2007**, *2*, 30.
[19] U. Aslam, S. Chavez, S. Linic, *Nat. Nanotechnol.* **2017**, *12*, 1000.
[20] M. L. Brongersma, N. J. Halas, P. Nordlander, *Nat. Nanotechnol.* **2015**, *10*, 25.
[21] L. Zhou, J. M. P. Martirez, J. Finzel, C. Zhang, D. F. Swearer, S. Tian, H. Robatjazi, M. Lou, L. Dong, L. Henderson, P. Christopher, E. A. Carter, P. Nordlander, N. J. Halas, *Nat. Energy* **2020**, *5*, 61.
[22] A. Naldoni, Z. A. Kudyshev, L. Mascaretti, S. P. Sarmah, S. Rej, J. P. Froning, O. Tomanec, J. E. Yoo, D. Wang, Š. Kment, T. Montini, P. Fornasiero, V. M. Shalaev, P. Schmuki, A. Boltasseva, R. Zbořil, *Nano Lett.* **2020**, *20*, 3663.
[23] A. V. Kildishev, A. Boltasseva, V. M. Shalaev, *Science* **2013**, *339*, 1232009.
[24] A. S. Solntsev, G. S. Agarwal, Y. S. Kivshar, *Nat. Photonics* **2021**, *15*, 327.
[25] L. Hüttenhofer, M. Golibrzuch, O. Bienek, F. J. Wendisch, R. Lin, M. Becherer, I. D. Sharp, S. A. Maier, E. Cortés, *Adv. Energy Mater.* **2021**, *11*, 2102877.
[26] R. Yalavarthi, L. Mascaretti, Z. A. Kudyshev, A. Dutta, S. Kalytchuk, R. Zbořil, P. Schmuki, V. M. Shalaev, Š. Kment, A. Boltasseva, A. Naldoni, *ACS Appl. Energy Mater.* **2021**, *4*, 11367.
[27] A. Boltasseva, V. M. Shalaev, *ACS Photonics* **2019**, *6*, 1.
[28] G. T. Forcherio, D. R. Baker, J. Boltersdorf, A. C. Leff, J. P. McClure, K. N. Grew, C. A. Lundgren, *J. Phys. Chem. C* **2018**, *122*, 28901.
[29] S. Deng, B. Zhang, P. Choo, P. J. M. Smeets, T. W. Odom, *Nano Lett.* **2021**, *21*, 1523.
[30] V. G. Kravets, A. V. Kabashin, W. L. Barnes, A. N. Grigorenko, *Chem. Rev.* **2018**, *118*, 5912.
[31] M. S. Bin-Alam, O. Reshef, Y. Mamchur, M. Z. Alam, G. Carlow, J. Upham, B. T. Sullivan, J.-M. Ménard, M. J. Huttunen, R. W. Boyd, K. Dolgaleva, *Nat. Commun.* **2021**, *12*, 974.
[32] Y. Zhao, X. Li, J. M. Schechter, Y. Yang, *RSC Adv.* **2016**, *6*, 5384.
[33] P. S. Deshpande, V. R. Chaudhari, B. L. V. Prasad, *Energy Technol.* **2020**, *8*, 1900955.
[34] U. Aslam, V. G. Rao, S. Chavez, S. Linic, *Nat. Catal.* **2018**, *1*, 656.
[35] X. Zhang, C. Huang, M. Wang, P. Huang, X. He, Z. Wei, *Sci. Rep.* **2018**, *8*, 10499.
[36] M. Valenti, A. Venugopal, D. Tordera, M. P. Jonsson, G. Biskos, A. Schmidt-Ott, W. A. Smith, *ACS Photonics* **2017**, *4*, 1146.
[37] R. Kamarudheen, G. W. Castellanos, L. P. J. Kamp, H. J. H. Clercx, A. Baldi, *ACS Nano* **2018**, *12*, 8447.
[38] Y. Kim, J. G. Smith, P. K. Jain, *Nat. Chem.* **2018**, *10*, 763.
[39] G. Tagliabue, J. S. DuChene, M. Abdellah, A. Habib, D. J. Gosztola, Y. Hattori, W.-H. Cheng, K. Zheng, S. E. Canton, R. Sundararaman, J. Sá, H. A. Atwater, *Nat. Mater.* **2020**, *19*, 1312.
[40] R. Sundararaman, P. Narang, A. S. Jermyn, W. A. Goddard III, H. A. Atwater, *Nat. Commun.* **2014**, *5*, 5788.
[41] J. B. Khurgin, *Nanophotonics* **2020**, *9*, 453.
[42] A. O. Govorov, H. Zhang, Y. K. Gun'ko, *J. Phys. Chem. C* **2013**, *117*, 16616.
[43] P. Christopher, M. Moskovits, *Annu. Rev. Phys. Chem.* **2017**, *68*, 379.
[44] G. Chen, M. Sun, J. Li, M. Zhu, Z. Lou, B. Li, *Nanoscale* **2019**, *11*, 18874.
[45] B. Seemala, A. J. Therrien, M. Lou, K. Li, J. P. Finzel, J. Qi, P. Nordlander, P. Christopher, *ACS Energy Lett.* **2019**, *4*, 1803.
[46] J. S. DuChene, G. Tagliabue, A. J. Welch, W.-H. Cheng, H. A. Atwater, *Nano Lett.* **2018**, *18*, 2545.
[47] E. Pensa, J. Gargiulo, A. Lauri, S. Schlücker, E. Cortés, S. A. Maier, *Nano Lett.* **2019**, *19*, 1867.
[48] E. Oksenberg, I. Shlesinger, A. Xomalis, A. Baldi, J. J. Baumberg, A. F. Koenderink, E. C. Garnett, *Nat. Nanotechnology* **2021**, *16*, 1378.
[49] M. J. Kale, T. Avanesian, H. Xin, J. Yan, P. Christopher, *Nano Lett.* **2014**, *14*, 5405.
[50] M. Bonn, S. Funk, C. Hess, D. N. Denzler, C. Stampfl, M. Scheffler, M. Wolf, G. Ertl, *Science* **1999**, *285*, 1042.
[51] S. Rej, L. Mascaretti, E. Y. Santiago, O. Tomanec, Š. Kment, Z. Wang, R. Zbořil, P. Fornasiero, A. O. Govorov, A. Naldoni, *ACS Catal.* **2020**, *10*, 5261.
[52] A. J. Wilson, P. K. Jain, *Accounts Chem. Res.* **2020**, *53*, 1773.
[53] P. B. Johnson, R. W. Christy, *Phys. Rev. B* **1974**, *9*, 5056.
[54] H. Reddy, U. Guler, A. V. Kildishev, A. Boltasseva, V. M. Shalaev, *Opt. Mater. Express* **2016**, *6*, 2776.